Journal of Alloys and Compounds 509 (2011) 8065–8072

Contents lists available at ScienceDirect

Journal of Alloys and Compounds

journal homepage: www.elsevier.com/locate/jallcom

Synthesis and functional properties of the $Ni_{1-x}Mn_xFe_2O_4$ ferrites

M. Airimioaei [a], C.E. Ciomaga [b,*], N. Apostolescu [c], L. Leontie [b], A.R. Iordan [a], L. Mitoseriu [b,*], M.N. Palamaru [a]

[a] Faculty of Chemistry, Al. I. Cuza University, Iasi 700506, Romania
[b] Faculty of Physics, Al. I. Cuza University, Iasi 700506, Romania
[c] Faculty of Chemical Engineering and Environmental Protection, Gheorghe Asachi Technical University of Iasi, 700050, Romania

ARTICLE INFO

Article history:
Received 10 November 2010
Received in revised form 5 May 2011
Accepted 10 May 2011
Available online 18 May 2011

Keywords:
Ceramics
Sol–gel processes
X-ray diffraction
Dielectric response
Magnetic measurements

ABSTRACT

Nanocrystalline $Ni_{1-x}Mn_xFe_2O_4$ ($x = 0$; 0.17; 0.34; 0.5) ferrite powders were successfully synthesized using the sol–gel combustion method, by using nitrates as cations source and citric acid ($C_6H_8O_7$) as combustion/chelating agent. The reaction advancement was observed by means of IR absorption spectroscopy, by monitoring two characteristic bands for the spinel compounds at about 600 cm^{-1} and 400 cm^{-1}, respectively. The as-synthesized powders were characterized by IR spectroscopy, X-ray diffraction (XRD) and scanning electronic microscopy (SEM). The magnetic study shows that the saturation magnetization decreases with increasing the Mn addition, as result of the particle size reduction. The dielectric properties were measured as a function of frequency in the range of 10 Hz to 1 MHz. The real part of permittivity has values of ~88 at 1 kHz and ~7 at 1 Hz for $x = 0$. An increasing dielectric permittivity with increasing the amount of Mn is observed. For all the investigated compositions, both the real and imaginary parts of permittivity decrease with frequency.

1. Introduction

Due to their magnetic and dielectric properties, the nanocrystalline spinels ferrites with the general formula MFe_2O_4 (M = Mn, Ni) are important materials with multiple applications, such as: magnetic recording media and magnetic fluids for storage and/or retrieval of information, catalysts, magnetically guided drug delivery, magnetic resonance imaging (MRI) enhancement, microwave absorbers, sensors and pigments [1].

Large-scale applications of ferrites with small particles have promoted the development of various chemical methods for the preparation of the nanosized spinel ferrites [2–9] as alternatives to the solid state reaction methods, which result in large agglomerated particles, with limited degree of homogeneity, and low sinterability [10]. The studies have shown that the synthesis protocol determines the structural characteristics of materials, which in turn, influence their magnetic and electrical properties.

Lately, a high importance is given by synthesis methods with low toxicity, or by economical methods in terms of energy consumption, enable to produce fine, nano-sized, single-crystalline and single phase powders. Spinel ferrites are generally synthesized using the standard ceramic technique [10] which implies high temperatures and leads to particles with small specific surface. In order to obtain ferrites with larger specific surface and higher degree of homogeneity, alternative methods like: co-precipitation [2,11], polymeric gel [3], hydrothermal [4], micro-emulsion [5], heterogeneous precipitation [6,12], sono-chemistry [7], combustion [8], sol–gel [9] methods, etc. were used.

In particular, the synthesis by combustion reaction technique has been shown to have great potential in the preparation of ferrites [13] and involves an exothermic and self-sustaining chemical reaction between the desired metal salts and a suitable organic fuel. The sol–gel self-combustion technique is a method that combines the chemical sol–gel process with the combustion process. Citric acid is often used as chelating agent and the obtained nitrate–citrate gel exhibits self-propagation combustion if ignited in air. This process was successfully used in producing a large variety of ferrites with homogeneous nanosized particles. It has also the advantages of autocombustion, use of inexpensive precursors, simple equipment and low temperatures for synthesis [14–16].

The $MnFe_2O_4$ has a spinel crystal structure (space group Fd3m), in which O^{2-} cations form a compact cubic structure, with Mn^{2+} and Fe^{3+} cations placed in two types of interstitial or crystallographic positions. These positions display a tetrahedral (denoted as A) and octahedral coordination (denoted as B) with respect with oxygen, and in this way their local symmetry is different. In the normal spinel structure, the bivalent ions (Mn^{2+} in $MnFe_2O_4$), occupy only the tetrahedral positions, while the trivalent ions (Fe^{3+} in $MnFe_2O_4$) populate the octahedral positions. In the inverse spinel

* Corresponding authors. Tel.: +40 232201102/2406; fax: +40 232201205.
E-mail addresses: cristina.ciomaga@uaic.ro, CrisFedor@stoner.phys.uaic.ro, crisfedor@yahoo.com (C.E. Ciomaga), lmtsr@uaic.ro (L. Mitoseriu).

0925-8388/$ – see front matter © 2011 Elsevier B.V. All rights reserved.
doi:10.1016/j.jallcom.2011.05.034

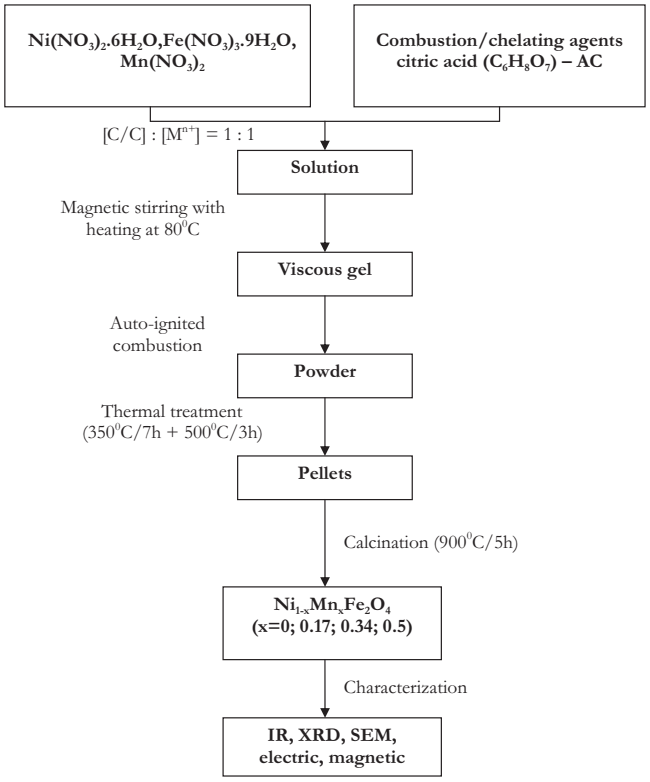

Fig. 1. The synthesis protocol flowchart for the preparation of $Ni_{1-x}Mn_xFe_2O_4$ with various compositions: $x = 0$; 0.17; 0.34; 0.5.

structure, the bivalent ions occupy half of the B positions, and the trivalent ions are placed in the rest of the B positions and in all A positions. In the $MnFe_2O_4$ ferrites obtained at high temperatures (>900 °C), 20% of the Mn^{2+} ions are migrating from A to B positions resulting in a ferrite with mixed spinel structure [17]. Using neutron diffraction, Ghazanfar et al. [18] measured the distribution of manganese ions among the tetrahedral and octahedral sites in $Mn_{1-x}Fe_{2-x}O_4$, and they found that 30% of the octahedral sites are occupied by Mn^{3+} with the distribution $Mn_{0,9}{}^{2+}Fe_{0,1}{}^{3+}[Mn_{0,6}{}^{3+}Fe_{1,6}{}^{3+}Fe_{0,1}{}^{2+}]O_4{}^{2-}$. This class forms the soft ferrites group, which is characterized by high magnetic permeability and low hysteresis losses [19].

Nickel ferrites $NiFe_2O_4$ belong to the category of the most important ferrites with inverse spinel structure with ferrimagnetic properties. For these ferrites the Fe^{3+} ions are placed on the tetrahedral sites and the Ni^{2+} ions are placed in octahedral sites [20].

The aim of this work was to study the structure, magnetic and dielectric properties of the nickel ferrites substituted by manganese: $Ni_{1-x}Mn_xFe_2O_4$ with compositions $x = 0$; 0.17; 0.34; 0.5 obtained by using the self-combustion method.

2. Sample preparation and experimental details

The $Ni_{1-x}Mn_xFe_2O_4$ ($x = 0$; 0.17; 0.34; 0.5) ferrite powders were prepared using the combustion reaction by using as cations source nitrates: $Ni(NO_3)_2{\cdot}6H_2O$, $Fe(NO_3)_3{\cdot}9H_2O$ and $Mn(NO_3)_2$ obtained in situ from metallic Mn and HNO_3 (20%), and citric acid $C_6H_8O_7$ as combustion agent. The citric acid is a low cost adequate ecological fuel and its decomposition generates high temperatures during the burning process, leading to the obtaining of the complete ferrite phase in external conditions.

The homogeneous solutions of nitrates were jellified in the presence of the combustion/chelating agents and the obtained gel was then thermally treated according to the synthesis protocol described in Fig. 1.

In order to monitor the spinel structure formation, FTIR spectroscopy was employed (with a Jasco 660 plus FTIR spectrophotometer using the KBr pellet).

To determine the changes which occur during the heating process the TG-EGA-FTIR apparatus consisted of a Diamond TG/DTA (Perkin Elmer) thermo-balance, a Spectrum 100 (Perkin Elmer) FTIR spectrophotometer, a TG-FTIR (Perkin Elmer) gas transfer accessory (1.6 m stainless steel 1.5 mm tube heated at 220 °C) and a heated gas cell of 100 mm length with KBr windows (heated at 150 °C). The Spectrum TimeBase (Perkin Elmer) software records every 15 s a single spectrum within the 700–4000 cm^{-1}, at a resolution of 4 cm^{-1}. The analysis was run with 10 mg sample placed into a platinum crucible, under dynamic dry air atmosphere (100 mL min^{-1}) at a heating rate of 10 K min^{-1}, within the 30–900 °C temperature range.

X-ray diffraction measurements were used to investigate the phase purity of the spinel phase of $Ni_{1-x}Mn_xFe_2O_4$ ($x = 0$; 0.17; 0.34; 0.5) by using a Seifert diffractometer (type XRD 3003 PTS) with a CuK_α radiation ($\lambda = 1.5405$ Å). A VEGA TESCAN scanning electron microscope coupled with EDX was used to analyze the morphology and agglomeration tendency of the synthesized powders, as well as the microstructure of the resulted ceramics and to check the local stoichiometry of the samples. The permeability vs. frequency measurements in the frequency domain (1 MHz–3 GHz) at room temperature were realized by using an E4991A RF Impedance/Material Analyzer on toroidal ceramic samples with sizes of ~1.4 mm × 4 mm × 12 mm (thickness, inner diameter and outer diameter). In order to determine the M (H) hysteresis loops in the range 0–1.4 T (14,000 Oe), a Micro-MagTM magnetometer VSM (Vibrating Sample Magnetometer) model 3900 system from Princeton Measurements Co. was used. The dielectric properties vs. frequency in the 10 Hz–1 MHz frequency domain at room temperature were determined by performing complex impedance measurements with an Impedance/Gain-Phase analyser SOLARTRON 1260A. Ceramic samples were cut into plane-parallel geometry and placed inside a dielectric holder containing a guard ring, needed to reduce non-homogenous field edge. The real and imaginary part of the impedance at different frequencies were determined and then the permittivity vs. frequency dependence.

3. Results and discussion

3.1. Thermal analysis

In order to determine the appropriate heat treatment adequate for obtaining the spinel ferrites, a thermal analysis was firstly performed.

In the first stage of the gel formation, it was observed an emission of a brown gas, NO_2. After the jellifying phase, the obtained product was dried and thermally analyzed.

The thermal decomposition of the $x = 0$ ferrite (Fig. 2a) reveals that the process for obtaining the spinel ferrites is ending at about 400 °C heating after this temperature has no effect for the weight of the sample.

The components of released gaseous mixtures have been monitored and identified mostly on basis of their FTIR reference gas spectrum available on world wide web in the public spectrum library of NIST. In the FTIR spectra recorded at 189 °C (Fig. 2b), the presence of H_2O, CO_2 [21] and N_2O [22] is observed. The evolution of the absorption at characteristic wavenumber for these gases with the temperature is presented in Fig. 2c.

In agreement with the obtained results, for the ferrite formation, are proposed the following reaction sequences:

$$(1-x)Ni(NO_3)_2 + xMn(NO_3)_2 + 2Fe(NO_3)_3 + 3C_6H_8O_7 \xrightarrow{\text{temperature}} NO_2\uparrow$$

$$+\,\text{dry gel} \xrightarrow{\text{temperature}} Ni_{1-x}Mn_xFe_2O_4$$

$$+N_2O\uparrow + CO_2\uparrow + H_2O\uparrow$$

Three steps are present in the TG-EGA-FTIR analysis (Fig. 2a): the sample drying (below 150 °C), a decomposition of the nitrates and burning of the organic materials. Exothermic effect recorded on heat flow curve at the peak around 290 °C is about $\Delta H \sim -5000$ J/g.

As shown in Fig. 2(a, d–f) the thermal decomposition on synthesis of ferrites powders series is also divided into three steps. The first is a weight loss upon drying the sample (below 150 °C), and the moisture is released at this stage (10–12% low); this thermal effect is endothermic. The second stage is ranging between 150 and 262 °C (weight loss is about 21–25%). In this stage, on the DTG curves, the shape of the curve is depending on the composition: for

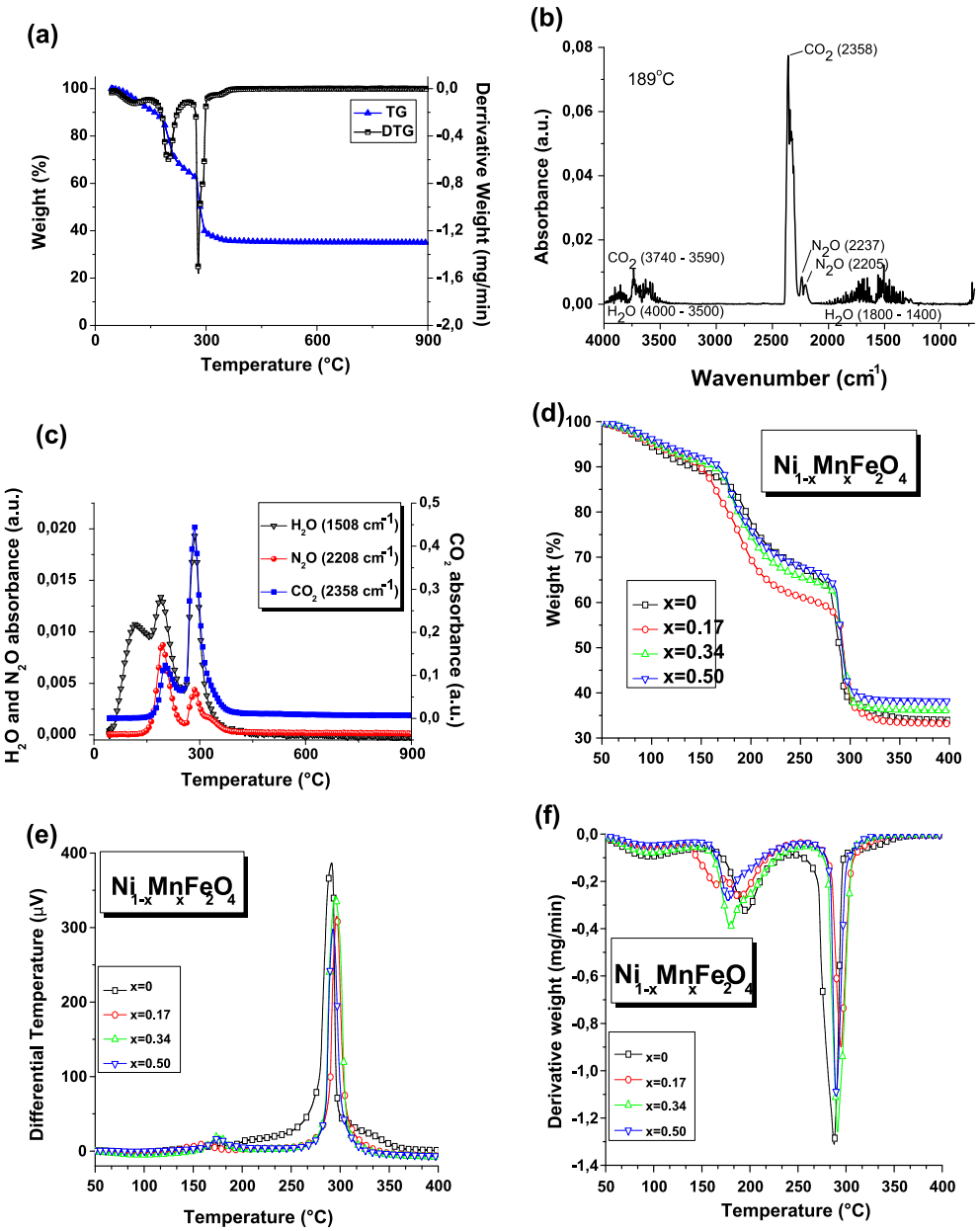

Fig. 2. The thermal analysis for the $Ni_{1-x}Mn_xFe_2O_4$ ($x = 0$; 0.17; 0.34; 0.5) ferrites: (a) simultaneous TG/DTA curves of the $x = 0$ ferrite in air flow; (b) FTIR spectrum of evolved gases from the $x = 0$ ferrite, measured at 189 °C by online coupled TG-EGA-FTIR system and identification of the gaseous components; (c) absorbance vs. temperature curves of identified gaseous species evolved from the $x = 0$ ferrite; (d) TG curves for $x = 0$; 0.17; 0.34; 0.5 ferrites; (e) DTA curves for synthesized ferrites and (f) DTG curves for synthesized ferrites.

the sample with $x = 0$, the peak is at ~199 °C and the thermal effect is endothermic; with the increase of x, a new peak at a lower temperature of 170–180 °C appears and the thermal effect in the DTA curve is exothermic. The mechanism of the decomposition in this stage is different for each precursor: for Mn an exothermic reaction and for the Ni an endothermic effect is found (Fig. 2).

The third stage is a fast thermal decomposition between 262 and 360 °C; weight loss is 28–29%. The reaction is strongly exothermic, the probe temperature rise quickly over the oven temperature in a very short time. After heating over 360 °C, the weight loss is insignificant and no thermal effect is observed on the DTA curve.

The thermal decomposition of the $x = 0$ ferrite (Fig. 2a) reveals that the process for obtaining the spinel ferrites is ending at about 400 °C heating after this temperature has no effect for the weight of the sample.

3.2. Infrared spectroscopy investigation

The formation of $Ni_{1-x}Mn_xFe_2O_4$ ($x = 0$; 0.17; 0.34; 0.5) spinel structure was monitored by using IR spectroscopy. In this scope the IR absorption spectra in different stages of the synthesis were recorded, taking also into consideration the information provided by the thermal analysis. The IR absorption spectra for the samples treated at 500 °C and 900 °C, respectively, are displayed in Figs. 3 and 4.

The IR absorption spectra recorded for the pre-sintered samples at 500 °C (Fig. 3) shows no absorption peaks characteristic for the nitrate or carbonate groups. It also can be remarked the presence of the absorption bands characteristic for the spinel structure around 600 cm^{-1}, and this behavior is also confirmed by the thermal analysis. Because the maximum from approximate 730 cm^{-1},

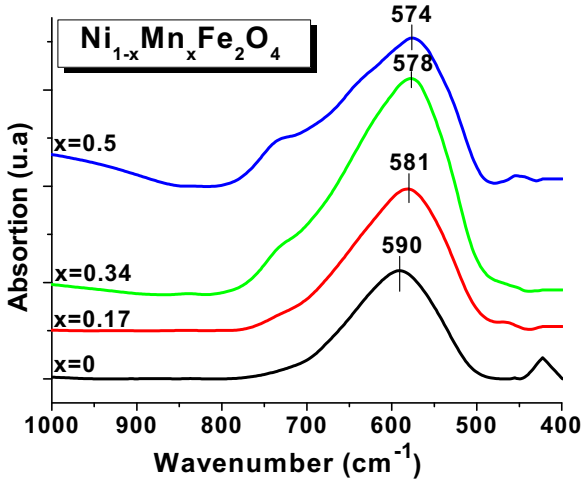

Fig. 3. IR spectra of $Ni_{1-x}Mn_xFe_2O_4$ ($x = 0$; 0.17; 0.34; 0.5) after thermal treatment at 500 °C/3 h.

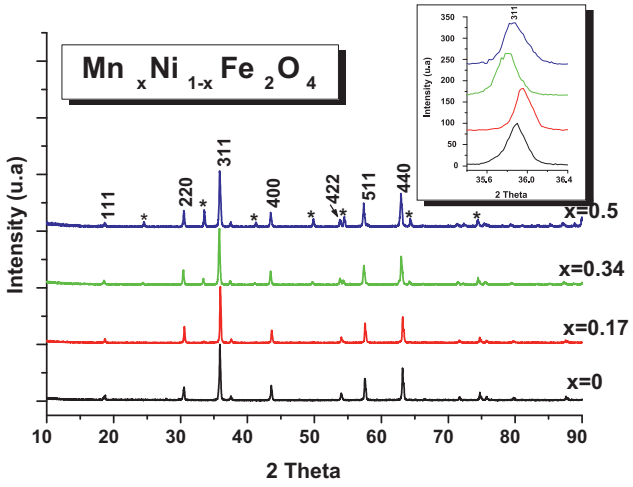

Fig. 5. XRD patterns of $Ni_{1-x}Mn_xFe_2O_4$ ($x = 0$; 0.17; 0.34; 0.5) ferrites after thermal treatment at 900 °C/5 h.

present at 500 °C, disappear after thermal treatment at 900 °C, this can be related to a partial disorder of the network, especially for the compositions $Ni_{1-x}Mn_xFe_2O_4$ with $x = 0.34$ and 0.5.

The spectra recorded for the samples sintered at 900 °C (Fig. 4) present two main absorption bands corresponding to the stretching vibrations around the values of 600 cm^{-1} and 400 cm^{-1}, respectively. The larger absorption band at ~600 cm^{-1} corresponds to the intrinsic vibration of tetrahedral complexes and the lower absorption band at ~400 cm^{-1} is attributed to the stretching vibrations of the octahedral complexes [23].

The shift of the absorption bands from higher to lower values can be attributed to the displacement of Fe, Mn and Ni ions related to the oxygen ions in the octahedral and tetrahedral sites, and due to this fact a modification of the Fe^{3+}–O^{2-} (M^{3+}–O^{2-}), respectively M^{2+}–O^{2-} distances takes place [24]. From the analysis of the IR absorption spectra, it is observed that the band from ~600 cm^{-1} shifts to lower wave numbers with increasing of Mn content. This indicates a lower degree of occupancy of tetrahedral sites with Fe^{3+} ions [25].

3.3. X-ray diffraction analysis

Fig. 5 shows the XRD patterns of $Ni_{1-x}Mn_xFe_2O_4$ ($x = 0$; 0.17; 0.34; 0.5) nanoparticles after the thermal treatment at 900 °C. All the characteristic peaks of the ferrite material are observed, with the most intense peak (3 1 1) at ~36°, which confirms the formation of the cubic spinel structure (JCPDS: 10-0325) [26]. We can see that with increasing of the Mn addition, the synthesis conditions promote the formation of Fe_2O_3 (JCPDS: 87-1166) and orthoferrite $MnFeO_3$ (JCPDS: 75-0894) as secondary phase, which is in agreement with other data reported in literature [27–29].

The average crystallite size of the $Ni_{1-x}Mn_xFe_2O_4$ ($x = 0$; 0.17; 0.34; 0.5) powders were determined by using the Debye–Scherrer relation:

$$D = \frac{0.9\lambda}{\beta \cos\theta}$$

where $\beta_{1/2}$ is the broadening of diffraction line measured at half maximum intensity (rad) and $\lambda = 1.5405$ Å. The major spinel peaks (3 1 1), (4 4 0), (5 1 1) and (2 2 0) were considered for calculations. As can be seen from Fig. 5, once with increasing of Mn content, the diffraction peaks become broader. The crystallite size diminishes when increasing the Mn substitution from ~50 nm for $x = 0$ to ~40 nm for $x = 0.50$.

The refinement of the structures (Fig. 6) was carried out with the GSAS program, developed by Larson and Von Dreele, from X-ray powder diffraction data. The diffraction profiles were modeled by using a multiterm Simpson's rule integration of the pseudo-Voigt function.

The Rietveld analysis provides accurate information on the exact amount of additional phases, $MnFeO_3$ and Fe_2O_3, from ferrite samples (Table 1).

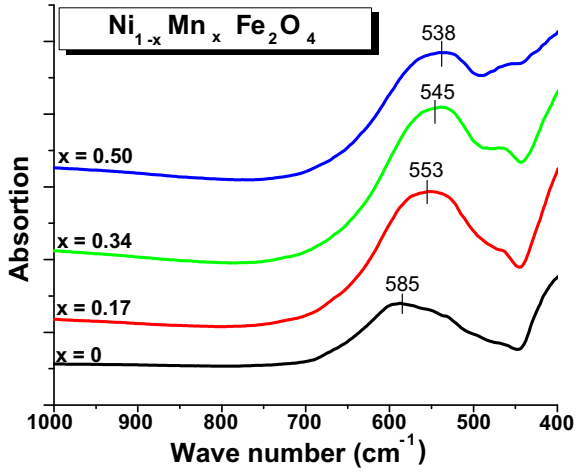

Fig. 4. The IR spectra of $Ni_{1-x}Mn_xFe_2O_4$ ($x = 0$; 0.17; 0.34; 0.5) ferrites after thermal treatment at 900 °C/5 h.

3.4. Microstructural characterization

The SEM images of two $Ni_{1-x}Mn_xFe_2O_4$ powder compositions after the thermal treatment at 900 °C are presented in Fig. 7a and b. The micrographs show the formation of soft agglomerates (easy de-agglomeration) with irregular morphology constituted of quite fine particles. The secondary electron image demonstrating a very

Table 1
The quantitative phase analysis using Rietveld refinement.

Samples	% Ferrite	% $MnFeO_3$	% $Fe2O_3$
$NiFe_2O_4$	100	0	0
$Mn_{0.17}Ni_{0.83}Fe_2O_4$	97	0	3
$Mn_{0.34}Ni_{0.66}Fe_2O_4$	89.4	0.2	10.4
$Mn_{0.5}Ni_{0.5}Fe_2O_4$	81.4	0.3	18.3

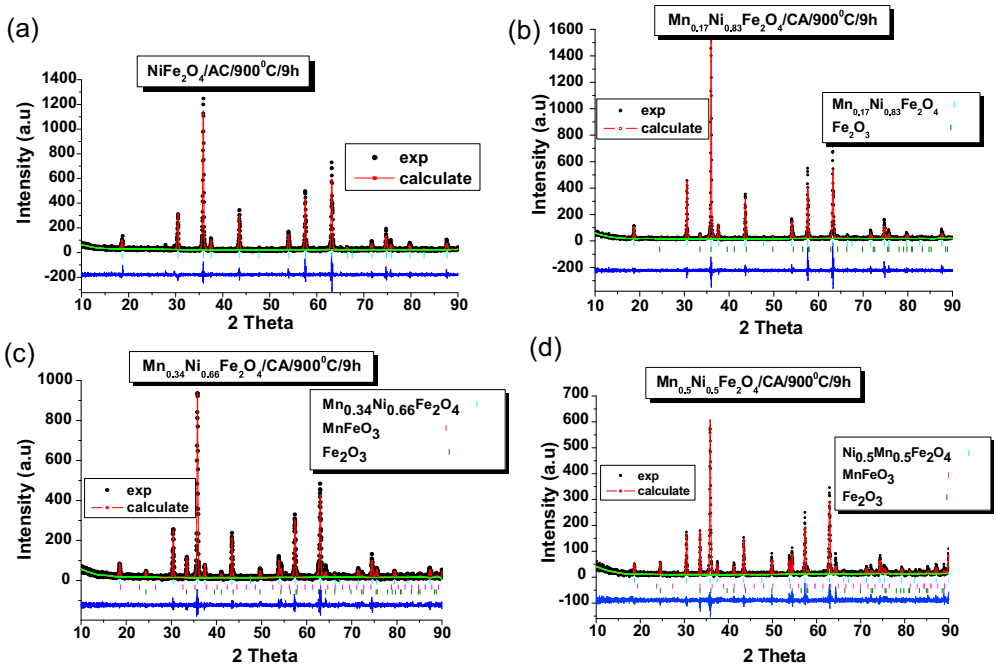

Fig. 6. Rietveld refinement pattern for sample: (a) $NiFe_2O_4$; (b) $Mn_{0.17}Ni_{0.83}Fe_2O_4$; (c) $Mn_{0.34}Ni_{0.66}Fe_2O_4$ and (d) $Mn_{0.5}Ni_{0.5}Fe_2O_4$.

good mixing resulted by this method of the in situ processing and spinel single phase at small x addition only. When increasing the amount of Mn, large agglomerates of spinel are formed together with finer particles belonging to the secondary phases (Fig. 7b). The local microprobe EDX analysis identified the larger blocks as being the majoritary spinel phase and the finer particles as belonging to the $MnFeO_3$ and Fe_2O_3 secondary phases. These results were confirmed by the XRD analysis.

3.5. Magnetic properties

Fig. 8 presents the M (H) loops at room temperature obtained for the $Ni_{1-x}Mn_xFe_2O_4$ ($x = 0$; 0.17; 0.34; 0.5) ceramics sintered at 900 °C/5 h. They show a typical ferrimagnetic character, with a strong non-linearity, very small coercive field below 60 Oe and saturation field of ~3 kOe. A decrease of the magnetic moment and saturation magnetization takes place with increasing Mn concentration, from $M_S = 50$ emu/g for $x = 0$ to $M_S = 39$ emu/g for $x = 0.50$. This property is in contrast with that observed in bulk ferrite, for which the saturation magnetization M_S increases with the Mn concentration, as reported by Hu et al. [30]. The present results can be explained by the gradual increase of the amount of orthoferrite and magnetite secondary phases and to the reduction of crystallite size, as the Mn concentration increases [27]. The coercitive field, H_C, slightly increases with increasing the amount of Mn from ~37.4 Oe to ~53.7 Oe for $x = 0$–0.5, respectively.

Fig. 9 shows the complex permeability spectra of the sintered $Ni_{1-x}Mn_xFe_2O_4$ ($x = 0$; 0.17; 0.34; 0.5) ferrites at room temperature. The ferrite samples present high values of permeability ($\mu_r' \sim 8$ for $x = 0$ to $\mu_r' \sim 27$ for $x = 0.5$ at 2 GHz) which are increasing with

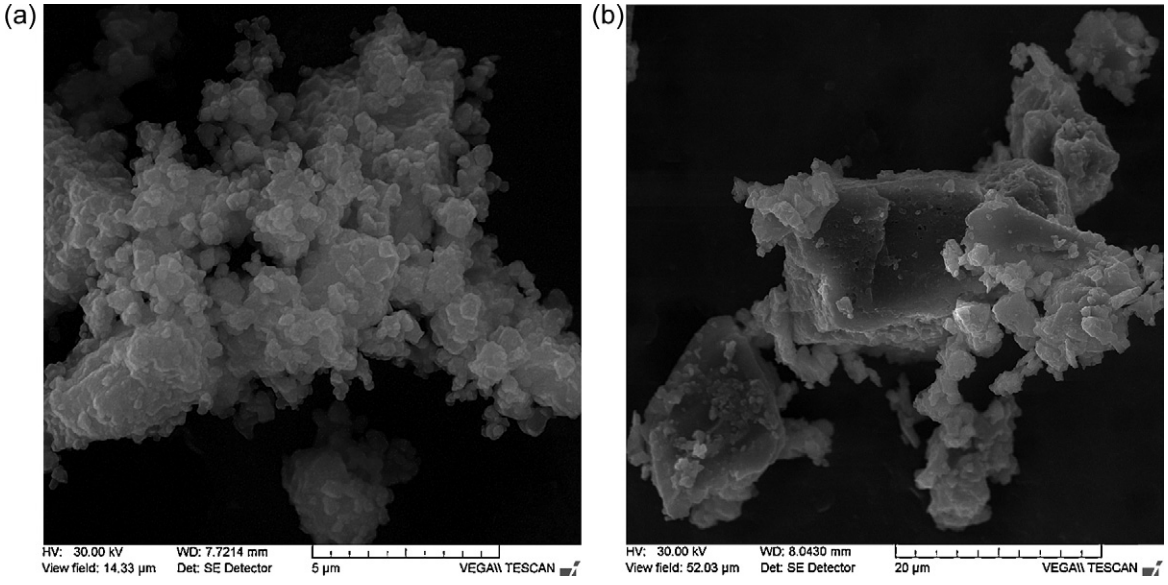

Fig. 7. SEM micrographs morphology of the $Ni_{1-x}Mn_xFe_2O_4$ powder sintered at 900 °C for: (a) $x = 0$ and (b) $x = 0.5$.

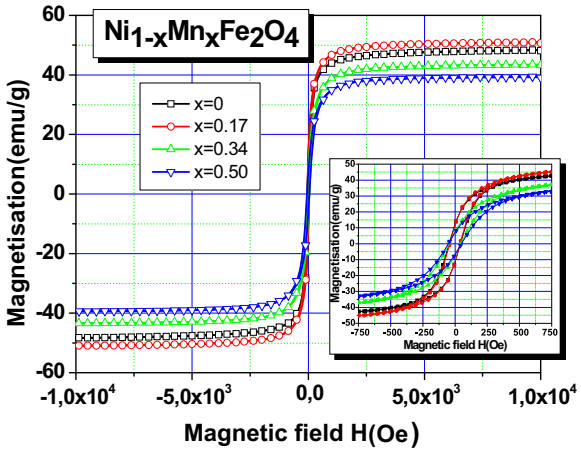

Fig. 8. Magnetic hysteresis loops M(H) at room temperature obtained for the $Ni_{1-x}Mn_xFe_2O_4$ ($x = 0$; 0.17; 0.34; 0.5) ceramics sintered at 900 °C/5 h.

Mn content. The high value of permeability together with low permittivity was reported by Lee et al. [31] in Mn and/or Co doping in Ni–Mn–Co ferrite, where the magnetic properties for high frequency microwave applications were investigated.

From Fig. 9 it can be observed that the real part of permeability became negative in the range 2.3–2.6 GHz, due to ferromagnetic resonance phenomena activated in this frequency domain. The peak of the intensity of resonance (imaginary part of permittivity) increases with increasing of Mn amount. This feature is attributed to the natural resonance of spin rotation and the vibrational resonance of the magnetic domain walls. It is known that above 2 GHz the domain wall motion cannot follow the field variation and thus, the frequency resonance corresponds to the spin resonance.

For polycrystalline ferrite, the permeability spectra are described by two types of magnetizing processes: spin rotation and domain wall motion [32]:

$$\mu = 1 + \chi_{spin} + \chi_{dw}$$

where χ_{spin} and χ_{dw} denote the magnetic susceptibility of spin and domain wall motion, respectively. In the sintered ferrite materials, the spin resonance frequency is proportional with saturation magnetization. Since the magnetization is decreasing with x, as shown in Fig. 8, it results that a domain wall contribution shifts the resonance towards higher frequencies when increasing x from 2.4 GHz to 2.54 GHz (Fig. 8a). This increase could also be explained by the increase of the demagnetization factor due to reducing crystallite size with x addition. An additional contribution to the anomalous high permeability and shift of the imaginary part maximum observed for $x = 0.50$ might be also attributed to the increasing amount of $MnFeO_3$ orthoferrite and Fe_2O_3 secondary phases.

3.6. Dielectric properties

The frequency dependence of the complex dielectric permittivity (ε', ε'') for all the ceramic samples was measured at room temperature. The real part of dielectric permittivity (Fig. 10a decreases with increasing frequency from 10 Hz to 1 MHz and show typical dielectric dispersion behavior (exponential decay), with a fast decrease of permittivity at low frequencies and slower at higher frequency. Besides the exponential decay of the permittivity vs. frequency trend, an additional polarization effect is found at high Mn addition (see the features in the frequency range of 10^3–10^4 Hz for $x = 0.50$ in Fig. 10a, which might be attributed to the presence of secondary phases with as larger amount as Mn addition (x) increases. The composition $x = 0$ has the highest values of real part of permittivity (at $f = 1$ kHz: $\varepsilon' \sim 88$) and decrease with increasing of frequency. For the composition $x = 0.17$, ε' present lower value by comparison with $x = 0$: $\varepsilon' \sim 15$ at $f = 1$ kHz. When increasing the amount of Mn from $x = 0.17$ to $x = 0.5$, the values of dielectric permittivity are increasing ($\varepsilon' \sim 70$ at $f = 1$ kHz). The high values of the real part of permittivity at low frequencies show a conductive behavior of these compositions, which originate in high values of the dielectric losses ($\tan\delta > 1$) at room temperature (Fig. 10b). At high frequencies above 10 kHz, the losses of all the compositions reduce below unity. The composition $x = 0.17$ presents the lowest losses in overall frequency range and is a good dielectric above 1 kHz ($\tan\delta < 1.5\%$ for $f > 1$ kHz).

The frequency dependence of the ac electrical conductivity is shown in Fig. 10c. For all the compositions, σ_{ac} increases with the applied field frequency. This can be associated with an increase in the hopping frequency of the charge carriers between Fe^{2+} and Fe^{3+} in the octahedral sites, as suggested in Refs. [16–19,33,34]. The frequency-dependent conductivity results at room temperature presents an almost zero conduction at low frequency (up to 10 kHz) for the compositions with $x = 0.17$, 0.34 with a large increasing for the frequency range 10^5–10^6 Hz, for all compositions.

Similar dielectric properties were often reported for other spinel ferrites [16–19,34] and are determined by the Maxwell–Wagner interfacial polarization phenomena [35–37], which are dominant at low frequencies. The polarization is the results of electron exchange

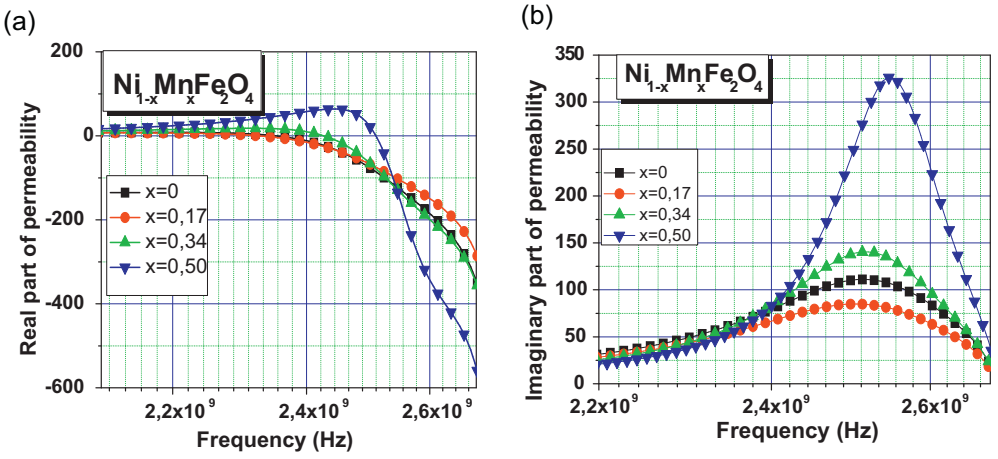

Fig. 9. Complex permeability of $Ni_{1-x}Mn_xFe_2O_4$ ($x = 0$; 0.17; 0.34; 0.5) ferrites at room temperature vs. frequency: (a) real part of permeability and (b) imaginary part of permeability.

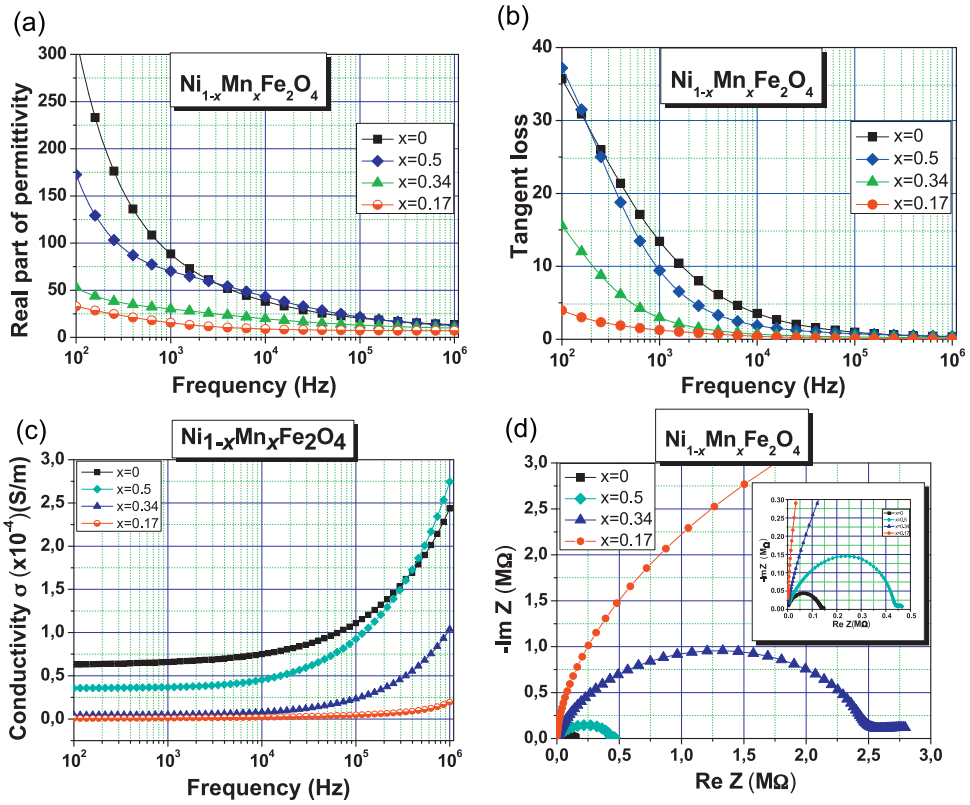

Fig. 10. Dielectric properties of the $Ni_{1-x}Mn_xFe_2O_4$ ($x = 0$; 0.17; 0.34; 0.5) ferrite ceramics at room temperature: (a) real part of permittivity vs. frequency; (b) tangent loss vs. frequency; (c) Ac-conductivity vs. frequency and (d) complex impedance plot.

between the ferrous and ferric ions $Fe^{2+} \leftrightarrow Fe^{3+} + e^-$, which gives rise to local electron displacements in the direction of the applied external field. Similarly, the $Mn^{3+} \leftrightarrow Mn^{2+} + e^+$ reaction gives an amount of holes (e^+) in the octahedral sites that ensure local displacements in the opposite direction with respect to the external applied field. The above displacements are responsible for the polarizability and macroscopic dielectric properties of the ceramic ferrites under consideration.

It seems that by increasing Mn addition, a tendency to reduce the losses exist (which manifests by the reduction of losses in $x = 0.17$ by comparison with $x = 0$ in overall frequency range), which might be related to the electron–hole partial compensation effects. However, further Mn addition increase result in the formation of higher amounts of secondary phases, whose contribution give rise to a further increase of the losses. In order to track down more realistic conclusions on the dielectric properties of $Ni_{1-x}Mn_xFe_2O_4$ ferrites, the synthesis parameters should be adjusted to produce pure single-phase ceramics in a large range of Mn addition.

From electrical point of view, the present $Ni_{1-x}Mn_xFe_2O_4$ ceramics under investigation are highly inhomogeneous systems, particularly for higher Mn addition, where the presence of secondary phases becomes predominant. This is also demonstrated by the complex impedance analysis (Fig. 10d). It is noticed that while $x = 0$ and $x = 0.17$ compositions show a single impedance arch, the impedance plots for $x = 0.34$ and $x = 0.50$ compositions reveal in their impedance diagram multiple components. Such a behavior is determined by the heterogeneous electrical properties at the microscopic level, i.e. to different electrical properties (resistivity, permittivity) inside the ceramic body, which might be attributed to secondary phases and intergrain interphases. The center of such arches is placed on the real axis and the complex impedance can be described by equivalent complex RC circuits [38]. The size of the semicircle changes with the number of components, with grain size and with the number of grains. The presence of a single semicircular arc obtained at higher frequencies corresponds to the electrical conduction determined by the interior of the ceramic grains of the majoritary phase. The diameter of the semicircle corresponds to the resistance of the grain [39]. As the Mn increases, the diameter of the semicircle decreases, indicating a reduction of the grain interior resistance. Thus, the total impedance (Z', the real axis intercepts at low frequency side) and imaginary component of complex impedance Z'' of all samples decreases with increase of Mn amount ($x = 0.17$, 0.34 and 0.5). As mentioned before, a more detailed impedance spectroscopy study in a large range of temperatures should be further performed to high purity ceramics in order to better attribute to a microscopic entity (grain core, grain boundary, defects, etc.), the observed impedance components.

4. Conclusions

The sol–gel combustion method, using nitrates as cations source and citric acid ($C_6H_8O_7$) as combustion/chelating agent offers a convenient synthetic route to prepare nanosized $Ni_{1-x}Mn_xFe_2O_4$ ($x = 0$; 0.17; 0.34; 0.5) ferrite powders.

The infrared (FTIR) spectroscopy, X-ray diffraction (XRD) and scanning electronic microscopy (SEM), confirm the formation of the $Ni_{1-x}Mn_xFe_2O_4$ ($x = 0$; 0.17; 0.34; 0.5) ferrites powders with the spinel structure, without secondary phases as α-Fe_2O_3 and Fe_3O_4. For higher Mn amount, besides the spinel phase, amounts of $MnFeO_3$ secondary phase are observed.

The magnetic properties as a function on composition are discussed. These results showed that with increasing Mn amount the saturation magnetization decrease and the value of coercitive field increase. Composition-dependent ferromagnetic resonance was found around 2.5 GHz. A dielectric frequency dispersion and conductivity determined by the contribution of the electron–hole

hopping mechanism were found. The complex impedance representation (Z'' vs. Z') reveal inhomogeneous ceramic ferrites and that due to the increasing of Mn addition. The compositions with $x = 0$ and $x = 0.17$ present a single impedance arch instead of $x = 0.34$ and $x = 0.50$ which are presented more than one components. The complex impedance spectra showed an evident inhomogeneity with increasing of Mn amount as due to distinct components of the ceramics with different resistivity and permittivity characteristics, possible attributed to the grain bulk, grain boundary, defects, etc. The ceramic sample with $x = 0.17$ is an optimum composition for which good magnetic and dielectrical properties are obtained. From magnetic and electric measurements resulted relatively high values of permeability ($\mu' \sim 20$ at 2 GHz) and low values of dielectric permittivity in the range kHz–MHz ($\varepsilon' \sim 70$ for $f = 1$ kHz in case of $x = 0.5$). Thus, after an improvement of the synthesis process and the elimination of the secondary phases the $Ni_{1-x}Mn_xFe_2O_4$ ferrite can be considered as promising materials for chip device application in the range of MHz and GHz, respectively.

Acknowledgement

This work was supported by CNCSIS-UEFISCSU, project number PN II-RU TE code 187/2010.

References

[1] M. Safarik, Safarikova, Magnetic nanoparticles and biosciences, in: H. Hofmann, Z. Rahman, U. Schubert (Eds.), Nanostructured Materials, Springer, Vienna, 2002, pp. 1–23.
[2] Y. Cesteros, P. Salagre, F. Medina, J. Eduardo Sueiras, Chem. Mater. 12 (2000) 331–335.
[3] W. Li, J. Li, J. Guo, J. Eur. Ceram. Soc. 23 (2003) 2285–2289.
[4] Z. Chen, E. Shi, Y. Zheng, W. Li, N. Wu, W. Zhong, Mater. Lett. 56 (2002) 601–605.
[5] C.R. Vestal, Z.J. Zhang, J. Solid State Chem. 175 (2003) 59–62.
[6] G. Li, X. Huang, M. Ruan, J. Guo, Ceram. Int. 28 (2002) 165–169.
[7] P. Jeevanandam, Y. Koltypin, A. Gedanken, Mater. Sci. Eng. B 90 (2002) 125–132.
[8] T. Mimani, J. Alloys Compd. 315 (2001) 123–128.
[9] C.O. Arean, M.P. Mentruit, A.J. Lopez, J.B. Parra, Colloids Surf. A 180 (2001) 253–258.
[10] J.M. Fernandez Colinas, C. Otero Arean, J. Solid State Chem. 109 (1994) 43–46.
[11] T. Jahanbina, M. Hashima, K. Amin Matoria, S. Bawa Waje, J. Alloys Compd. 503 (2010) 111–117.
[12] A. Angermann, J. Töpfer, K.L. da Silva, K.D. Becker, J. Alloys Compd. 508 (2010) 433–439.
[13] A.C.F.M. Costa, R.T. Lula, R.H.G.A. Kiminami, L.F.V. Gama, A.A. de Jesus, H.M.C. Andrade, J. Mater. Sci. 41 (2006) 4871–4875.
[14] Z.X. Yue, J. Zhou, L.T. Li, H.G. Zhang, Z.L. Gui, J. Magn. Magn. Mater. 208 (2000) 55–60.
[15] M.K. Shobana, S. Sankar, V. Rajendran, J. Alloys Compd. 472 (2009) 421–424.
[16] S.A. Seyyed Ebrahimi, J. Azadmanjiri, J. Non-Cryst. Solids 353 (2007) 802–804.
[17] J.M. Hastings, et al., Phys. Rev. B 104 (1956) 328–331.
[18] U. Ghazanfar, S.A. Siddigi, G. Abbas, J. Mater. Sci. Eng. B 118 (2005) 84–86.
[19] M.A. Ahmed, N. Okasha, S.I. El-Dek, Nanotechnology, vol. 19, IOP Publishing, 2008, pp. 065603–065608.
[20] S. Maensiri, C. Masingboon, B. Boonchom, S. Seraphin, Scripta Mater. 56 (2007) 797–800.
[21] NIST Chemistry Webbook Standard Reference Database, http://webbook.nist.gov/chemistry.
[22] J. Madarász, I.M. Szilágyi, F. Hangeb, G. Pokol, J. Anal. Appl. Pyrolysis 72 (2004) 197–201.
[23] R.D. Waldron, Phys. Rev. 9 (1955) 1727–1735.
[24] A.K. Ghatage, S.C. Choudhari, S.A. Patil, J. Mater. Sci. Lett. 15 (1996) 1548.
[25] M.D. Shultz, M.J. Allsbrook, E.E. Carpenter, J. Appl. Phys. 101 (2007) 9M518.
[26] R.C. Kambale, P.A. Shaikh, S.S. Kamble, Y.D. Kolekar, J. Alloys Compd. 478 (2008) 599–603.
[27] D.R. Sharma, Rashi Mathur, S.R. Vadera, N. Kumar, T.R.N. Kutty, J. Alloys Compd. 358 (2003) 193–204.
[28] E.M. Ewais, M.M. Hessien, A.A. El-Geassy, J. Aust. Ceram. Soc. 44 (2008) 57–62.
[29] M.M. Rashad, Mater. Sci. Eng. B 127 (2006) 123–129.
[30] J. Hu, H. Qin, Y. Wang, Z. Wang, S. Zhang, Solid State Commun. 115 (2000) 233–235.
[31] J.J. Lee, S. Bae, Y.K. Hong, J. Jalli, G.S. Abo, W.M. Seong, S.H. Park, C.J. Choi, J.G. Lee, J. Appl. Phys. 105 (2009) 07A514.
[32] T. Tsutaoka, M. Ueshima, T. Tokunaga, T. Nakamura, K. Hatakeyama, J. Appl. Phys. 78 (1995) 3983–3991.
[33] J. Alam, U. Riaz, S. Ahmad, J. Magn. Magn. Mater. 314 (2007) 93–99.
[34] L.J. Berchmans, M.P.I. Devi, K. Amalajyothi, Int. J. Self-Propag. High-Temp. Synth. 18 (2009).
[35] K.W. Wagner, Ann. Phys. (Leipzig) 40 (1913) 53.
[36] A. von Hippel, Dielectrics and Waves, Wiley, NY, 1954.
[37] M. Atif, M. Nadeem, R. Grössinger, R. Sato Turtelli, J. Alloys Compd. 509 (2011) 5720–5724.
[38] A.K. Jonscher, Dielectric Relaxation in Solids, Chelsea Dielectric Press, London, 1983.
[39] H. Ya, R.B. Jackman, P. Hing, J. Appl. Phys. 94 (2003) 7878–7882.